

Cone-based electrical resistivity tomography

Adam Pidlisecky¹, Rosemary Knight¹, and Eldad Haber²

ABSTRACT

Determining the 3D spatial distribution of subsurface properties is a challenging, but critical, part of managing the cleanup of contaminated sites. We have developed a minimally invasive technology that can provide information about the 3D distribution of electrical conductivity. The technique, cone-based electrical resistivity tomography (C-bert), integrates resistivity tomography with cone-penetration testing. Permanent current electrodes are emplaced in the subsurface and used to inject current into the subsurface region of interest. The resultant potential fields are measured using a surface reference electrode and an electrode mounted on a cone penetrometer. The standard suite of cone penetration measurements, including high-resolution resistivity logs, are also obtained and are an integral part of the C-bert method. C-bert data are inverted using an inexact Gauss-Newton algorithm to produce a 3D electrical conductivity map. A major

challenge with the inversion is the large local perturbation around the measurement location, due to the highly conductive cone. As the cone is small with respect to the total model space, explicit modeling of the cone is cost prohibitive. We have developed a rapid method for solving the forward model which uses iteratively determined boundary conditions (IDBC). This allows us to generate a computationally feasible, preinversion correction for the cone perturbation. We assessed C-bert by performing a field test to image the conductivity structure of the Kidd 2 site near Vancouver, British Columbia. A total of nine permanent current electrodes were emplaced and five C-bert data sets were obtained, resulting in 6516 data points. These data were inverted to obtain a 3D conductivity image of the subsurface. Furthermore, we demonstrated, using a synthetic experiment, that C-bert can yield high quality electrical conductivity images in challenging field situations. We conclude that C-bert is a promising new imaging technique.

INTRODUCTION

One of the main challenges in the cleanup and management of a contaminated site is developing an accurate model of the subsurface. Such a model ideally contains information about the location of contaminants, and information about the subsurface properties controlling the long-term fate and transport of the contaminants. Borehole-based electrical resistivity tomography (ERT) is a geophysical method that increasingly is being used to assist in the development of subsurface models. ERT involves injecting current through a pair of electrodes in one borehole, and measuring the resulting potentials at numerous (tens to hundreds of) electrodes located in the same borehole, and in different boreholes. The measurements yield values of resistance that can be inverted to determine the subsurface electrical conductivity structure. The electrical conductivity structure has been used, for example, to infer the presence of a contaminant, with electrical conductivity different from that of the background envi-

ronment, (e.g., Daily and Ramirez, 1995; LaBrecque and Yang, 2001) and to obtain information about potential flow paths of contaminants by imaging the movement of conductive tracers (Slater et al., 2000; Versteeg et al., 2000; Kemna et al., 2002; Slater et al., 2002; Singha and Gorelick, 2005).

A critical problem with the use of borehole-based ERT is the requirement of boreholes. Boreholes are not desirable at many contaminated sites due to the fact that installation is expensive, time consuming, and risks the exposure of workers to contaminants. In addition, there is potential for mobilizing contaminants by creating, with the boreholes, new pathways in the subsurface. These issues have motivated us to develop an ERT system that does not require the use of boreholes, but uses a cone penetrometer to position a small number of subsurface current electrodes around the region of interest and to make potential field measurements between an electrode mounted on the cone and a surface reference electrode.

Manuscript received by the Editor June 29, 2005; revised manuscript received November 30, 2005; published online July 31, 2006.

¹Stanford University, Department of Geophysics, 2215 Mitchell Building, Stanford, California 94305. E-mail: apid@pangea.stanford.edu; rknight@pangea.stanford.edu.

²Emory University, Department of Mathematics and Computer Science, Mathematics and Science Building E414, Atlanta, Georgia 30322. E-mail: haber@maths.emory.edu.

© 2006 Society of Exploration Geophysicists. All rights reserved.

The cone penetrometer is a testing tool that was developed by geotechnical engineers for obtaining high-resolution depth logs of mechanical soil properties. A cone penetrometer, commonly referred to as a cone, is a 36-mm diameter steel rod, ~ 1 m long, with sensors mounted close to a cone-shaped tip. Cone penetration testing (CPT), i.e., using the cone for subsurface characterization, is a technique that is now widely used in the environmental and geotechnical engineering community (Campanella and Weemeees, 1990; Daniel et al., 1999). The technique is classified as minimally invasive, because instead of drilling a borehole to make subsurface measurements, a cone is pushed into unconsolidated materials using hydraulic rams mounted on a large truck, referred to as the cone truck. While the cone is being pushed, measurements are made with the sensors in a near-continuous fashion, with typical sampling every 2.5 cm. To reach the measurement depth of interest, 1-m sections of steel rod are added to the end of the cone. The maximum depth of investigation varies with the geologic environment, but is generally limited to ~ 100 m. CPT is an efficient, relatively inexpensive alternative to borehole installation and works extremely well in areas of alluvial and deltaic deposits consisting of clays, silts, or sands.

The standard cone penetrometer, as most commonly configured, is shown schematically in Figure 1a. This standard cone measures three separate ground properties: tip penetration resistance, friction sleeve resistance, and induced pore pressure, all of which are used to obtain information about subsurface stratigraphy. The accelerometers can be calibrated to function as deviation sensors so that the cone can be accurately located. However, in standard cone penetration testing the accelerometers are rarely used for this purpose, and therefore, the uncertainties associated with these measurements have not been well established.

Of use for identifying zones of anomalous electrical conductivity is the method referred to as resistivity cone penetrometer testing (RCPT), which uses a resistivity module containing two pairs of ring electrodes. What is referred to as the resistivity cone is shown schematically in Figure 1b and includes the resistivity module and the standard cone. To make a measurement, a high-frequency (~ 1000 Hz) AC current is injected into one pair of electrodes, and the voltage is measured across the same pair of electrodes (Lunne et al., 1997). Figure 1b shows the two electrode pairs; the measure-

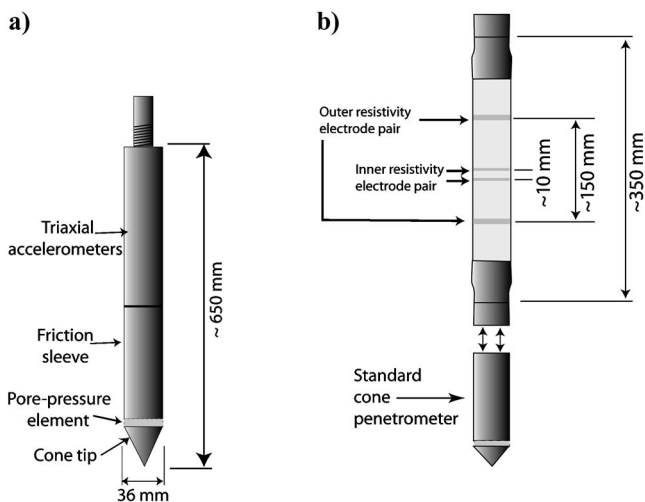


Figure 1. Schematics of (a) a standard cone penetrometer and (b) a resistivity cone.

ments are made using each electrode pair. The separation distance of the electrodes, along with the resistivity of the surrounding sediments, determines the volume sampled by the measurement. The module is 36.6 mm in diameter, which is slightly larger than the diameter of the standard cone to ensure good soil-electrode coupling. RCPT yields a high-resolution resistivity log in addition to the standard suite of cone data.

Recent work has highlighted the advantage of coupling geophysical imaging techniques with CPT. Narbutovskih et al. (1997) demonstrated the benefit of using CPT technology to emplace permanent vertical electrode arrays to monitor infiltration experiments using ERT. Their design proved successful, and showed the advantages in speed, cost, and safety over borehole-based ERT. Jarvis and Knight (2000, 2002) used a vertical seismic profile, obtained using accelerometers mounted on a cone, to constrain the inversion of 2D seismic shear-wave reflection data, thus improving the quality of the subsurface velocity model. Motivated by these previous studies, we have developed an acquisition system that combines ERT and CPT so as to gain the benefits realized by these studies.

In this paper, we present our new cone-based ERT (C-bert) system. We describe in detail a successful field test of this new approach, covering both the field procedures and the data processing/interpretation algorithms. We conclude with a synthetic example to demonstrate the potential of C-bert as a new way to obtain conductivity images of the subsurface.

DESCRIPTION OF FIELD SITE

The field experiment was conducted at the BC Hydro Kidd 2 research site in Richmond, British Columbia, Canada. The site is immediately adjacent to the Fraser River and has a zone of saltwater intrusion, extending well into the site (Neilson-Welch 1999). Kidd 2 is a very well-documented site, having been the focus of several geotechnical, geophysical, and hydrogeologic studies. Work on the site has included multiple cone penetrometer tests, multiple hydrogeologic well installations, various geophysical surveys, and the analysis of numerous core samples (Hofmann, 1997; Hunter et al., 1998; Jarvis et al., 1999; Neilson-Welch, 1999; Neilson-Welch and Smith, 2001; Jarvis and Knight, 2000, 2002).

The Kidd 2 site is composed of Holocene sediments deposited during the progradation of the Fraser River (Clague et al., 1983). Figure 2 is a cross section through the area around the Kidd 2 site, showing the five hydrostratigraphic units defined by Neilson-Welch and Smith (2001); these units are described in Table 1. Also shown in Figure 2 is the approximate extent of the saltwater intrusion. Imag-

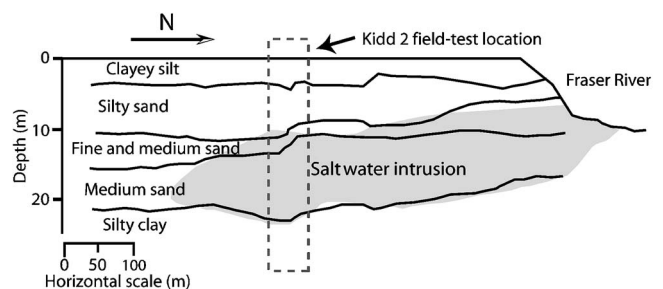


Figure 2. A cross section of the Kidd 2 site, with the approximate boundary of the saltwater intrusion overlaid (after Neilson-Welch and Smith, 2001).

ing the conductivity structure to a depth of 30 m was defined as the objective of our C-bert field test.

KIDD 2 C-BERT EXPERIMENT

Figure 3 is a schematic that illustrates the basic components of the C-bert system used at the field site. The survey area was 35×30 m (in the north-south and east-west directions, respectively). At nine locations on the grid, we used a cone truck to emplace permanent current electrodes in the subsurface. Once the current electrodes were in place, we pushed a resistivity cone into the ground and began the process referred to as C-bert. We acquired data in the standard RCPT mode, using the outer pair of electrodes on the resistivity module to obtain a 1D resistivity profile. At regular depth intervals (every 1–2 m), the cone was stopped and resistivity tomography measurements were made. To do this, current was injected into a pair of the permanent current electrodes. The potential drop was measured between a surface reference potential electrode, and the inner electrodes on the resistivity module (i.e., on the cone). This form of measurement was repeated for all independent current pairs. The cone was then pushed to the next interval, and the procedure repeated. This continued until the cone reached approximately 30 m. The truck was then moved, and the experiment repeated at a different location. Below, we describe in detail this field experiment.

Description of cone truck

We used the cone truck from the Department of Civil Engineering at the University of British Columbia (UBC). The UBC cone truck is a self-contained laboratory with all of the equipment needed for the calibration and deployment of the resistivity cone.

In an effort to reduce sources of electrical noise during C-bert measurements, the cone truck was electrically isolated from the ground and the cone rods. The hydraulic jack pads, which allow the truck to be lifted and leveled, are large steel plates, approximately $1 \times 2 \times 0.5$ m. In order to isolate the truck from the ground, we placed 2 mm thick PVC mats under the jack pads. Another concern was the two metal guides that keep the cone rod centered and aligned with the hydraulic rams. In order to isolate the truck from the cone rods plastic guides were used.

Table 1. Kidd 2 Hydrostratigraphic units (after Neilson-Welch and Smith, 2001).

Unit designation	Approximate depth (m)	Description
1	1–3.5	Clayey silt: clayey silt with trace fine sand laminations
2	3.5–9	Silty sand: fine- and medium-grained sand with interbeds of clayey silt, sandy silt, and fine sand
3	9–12	Fine and medium sand: includes interbeds of silt and fine sand
4	12–22	Medium sand: uniform medium sand with trace interbeds of silts
5	>22	Silty clay: includes thin laminations of silt

Description of the resistivity cone

The resistivity cone used in our study contained a standard cone and a resistivity module built by UBC. There are four brass ring electrodes on the module, arranged as two electrode pairs, one pair separated by ~ 10 mm, the other by ~ 150 mm. We used only the electrode pair separated by 150 mm to make the RCPT measurements. This electrode pair was calibrated using a technique similar to that described in Campanella and Weemees (1990). The resistivity cone was immersed in a $2 \times 2 \times 1.5$ m water tank. Sodium chloride (NaCl) was added to the tank; the resistivity of the water was measured with a conductivity probe; and the voltage was measured across the cone electrodes. This procedure was repeated ~ 20 times for different concentrations of NaCl. We observed a linear relationship between the cone voltage measurements and the probe-measured resistivity of the water, allowing us to define the calibration factor needed to obtain resistivity values from our cone measurements.

Making subsurface ERT measurements requires a potential electrode below the surface. A key part of the C-bert concept is the use of an electrode, pushed into the subsurface on the resistivity cone, as the subsurface potential electrode. We modified the resistivity module on the cone so that the inner electrode pair functioned as a single, isolated electrode. The C-bert system thus included the use of the outer electrodes on the resistivity module for resistivity logging, and the use of the inner electrodes for ERT measurements.

In addition to the two forms of resistance measurements, we acquired the standard suite of cone measurements. Once at the field site, the sensors in the standard cone were calibrated and the pore pressure sensor saturated as described in Lunne et al. (1997).

Design and emplacement of permanent electrodes

Figure 4 shows the plan of the survey grid, 35×30 m, covering the Kidd 2 site. On this plan view are shown the locations and depths of all the permanent electrodes. Also shown are the locations of 39 potential electrodes placed at the surface. These electrodes were

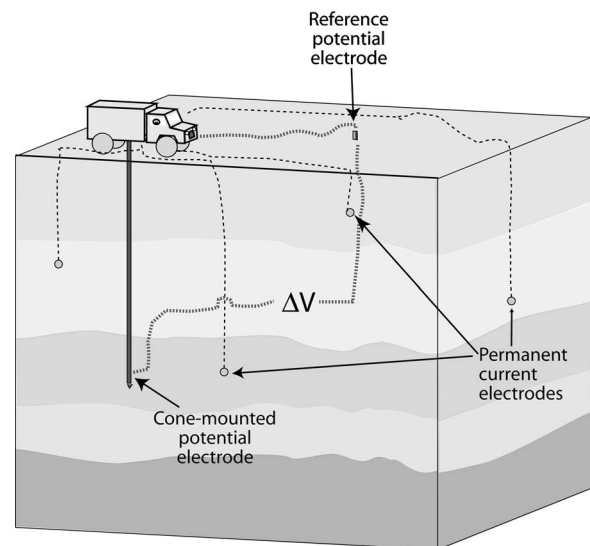


Figure 3. Schematic of a cone-based resistivity tomography system. The current electrodes are permanently emplaced prior to C-bert testing. Potential measurements are made using the cone-mounted potential electrode and can thus be made anywhere in the volume.

20 cm stainless steel stakes, hammered ~ 15 cm into the ground. These electrodes served to measure the potential field at the surface due to the permanent current electrodes. In addition, two of these electrodes (at the north-west and south-east corners of the grid) served as reference electrodes for the measurements made with the cone-mounted potential electrode.

The current electrodes, pictured in Figure 5a, were designed to be emplaced using the cone truck. Each electrode, machined out of 300-series stainless steel, has a conical tip with an apex angle of 60° , a maximum diameter of 41 mm and an overall length of 104 mm. A 12-gauge tinned copper wire was attached to the tip. The wire was held in place using two stainless setscrews. The resistance of the wire was ~ 5 mohm/m. The cable receptacle on the electrode was sealed using marine grade silicon sealer to minimize corrosion between the cable and the electrode. As shown schematically in Figure 5b, each electrode was inserted into a hollow cone rod that had a machined receptacle at one end. The electrode cable was threaded through the required number of cone rod sections, and the assembly was pushed into the subsurface with the electrode held in place by the force acting on the tip. Upon reaching the desired depth, the cone rod was retracted, leaving the electrodes in place.

Nine permanent current electrodes were emplaced at subsurface locations using the cone truck. As seen in Figure 4, two electrodes were placed at a depth of 5.5 m, in the upper fresh water zone; three

in the saltwater zone, between 15 and 16 m; three in the silty clay between 25 and 26 m; and one close to the interface between the saltwater zone and the silty clay. We were able to emplace all of the current electrodes in one day using the UBC cone truck (which is considerably slower than a commercial CPT rig). At the surface a small section of 6-in-diameter PVC casing was driven into the ground around the electrode cable and the casing capped with a screw-on lid. This protected the electrode leads, keeping them available for future repeat measurements.

Data acquisition

The initial phase of the C-bert data acquisition involved obtaining surface measurements with the 39 surface electrodes. This was done using a Syscal R1-Plus 200-watt resistivity meter. The unit cycled through the 36 independent subsurface current electrode pairs, while measuring the potential field at all the surface electrodes. These surface data were directly incorporated into the C-bert data set.

As shown in Figure 4, we collected C-bert data at five locations with the depth of the cone holes ranging from 23 to 30 m. At each location, the data acquisition involved two components: acquisition of the standard RCPT data (tip resistance, sleeve friction, induced pore pressure, and resistivity) and acquisition of the tomographic data using the permanent subsurface current electrodes, the surface reference electrodes, and cone-mounted electrode.

At each C-bert location, the resistivity cone was pushed into the ground using the cone truck, obtaining standard RCPT data, with measurements every 2.5 cm. These data yield high-resolution resistivity and stratigraphy depth logs. At all five of the C-bert locations, we successfully acquired the standard suite of CPT data, and at four of the locations we obtained high-resolution resistivity logs. In the first hole (C-bert 01), we experienced a problem with the resistivity log, so had to discard the data.

Every 1 m for C-bert 01, and every 2 m for C-bert 02-05, ERT measurements were made using the Syscal resistivity meter. All permanent subsurface current electrodes and reference surface potential electrodes, and the cone-mounted potential electrode were connected to the control unit. The unit was programmed so as to cycle, at each depth sampling location, through the 36 independent current electrode pairs, injecting current into each pair and measuring the potential drop between the surface reference potential electrodes and the cone-mounted potential electrode. This resulted in 72 measurements per depth interval. The full C-bert survey took four days to acquire 6516 data points. Error estimates for the data were obtained by stacking ten measurements for each datum, and recording

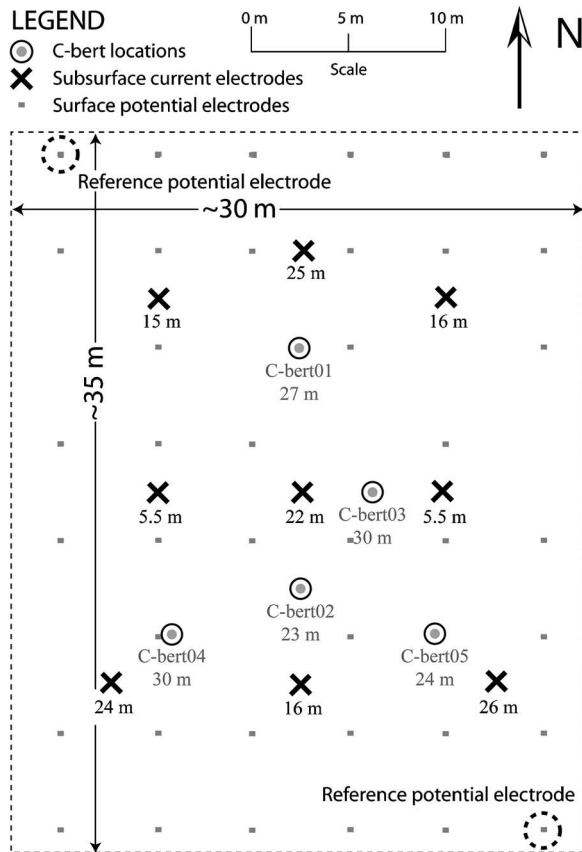


Figure 4. Kidd 2 survey map. The surface grid consisted of 39 electrodes. The locations of the nine permanent current electrodes are indicated by the X; the depth directly below the X is the depth of emplacement. C-bert data were acquired at five locations, labeled C-bert 01 through C-bert 05. The maximum depths reached in the C-bert data acquisition are listed below the location.

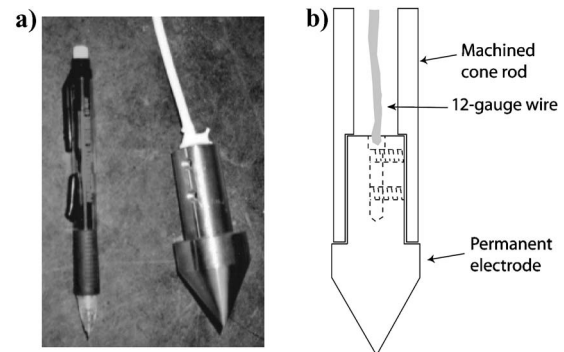


Figure 5. (a) Permanent current electrode. (b) Schematic of permanent electrode seated in deployment rod.

the standard deviation of these measurements. Typically, in resistivity experiments reciprocal measurements are used for determining the noise level. Reciprocal measurements involve switching the current and potential measurement pairs for each location. The reciprocal measurements should yield identical results, and any variation provides quantification of error (Binley et al., 2002). However, with the C-bert acquisition system, we are unable to inject current through the cone mounted electrode, because the wiring and circuits are not designed to accommodate large amounts of current, and thus, we could not obtain reciprocals. Table 2 is a compilation of the starting depths, depth intervals, and finishing depths of the survey.

FIELD RESULTS AND INTERPRETATION

Resistivity cone data

Inversion of ERT is a highly nonlinear optimization problem. As such, an accurate starting model greatly increases the rate and probability of convergence of the inversion. Furthermore, this starting model is often used as the reference model in the regularization term of the inversion, and thus it will greatly affect the appearance of the resulting inversion. The suite of RCPT data, which is acquired as part of the C-bert experiment, provides valuable information about the subsurface, that can be used to build a good starting model. Furthermore, the resistivity data can be used as constraints within the inversion.

Figure 6 is a plot of the RCPT logs superimposed on a cross section of the site. These data are from C-bert 05. The tip resistance, friction ratio (the percent ratio of sleeve friction to tip resistance), and induced pore pressure can be used to make interpretations of subsurface lithology. The most obvious lithologic feature in these logs is the top of the silty clay, which corresponds to a drop in tip resistance and an increase in friction ratio and induced pore pressure. More subtle is the boundary between the silty sand and the fine and medium sand. This boundary can be identified in both the friction ratio and pore pressure logs at approximately 10 m below the surface. Below this depth, the logs no longer show small-scale fluctuations, which would indicate the presence of silt. The resistivity log at this site is primarily an indicator of the extent of saltwater intrusion. From low values in the resistivity log, we see that the saltwater intrusion extends from approximately 10 to 23 m, i.e., the saltwater intrudes the units of fine and medium sand. For this particular site we had a considerable amount of a priori knowledge about the site, so the logs were not a necessity. It is clear, however, that the acquisition of these logs as part of the C-bert process is very useful for building a model of the subsurface.

Table 2. Testing depths for the tomography component of the C-bert experiment.

	Starting depth (m)	Maximum depth (m)	Depth interval (m)
C-bert 01	3	27	1
C-bert 02	2	20.5	2
C-bert 03	4	30	2
C-bert 04	4	30	2
C-bert 05	2.25	24	2

ERT forward modeling

ERT experiments yield a series of voltage measurements in response to a series of known input currents. From these data, we need to invert for the subsurface conductivity structure. The first step in this process involves the development of a mathematical framework, the forward model, that relates the recorded data to the conductivity structure:

$$-\nabla \cdot (\sigma \nabla \phi) = I(\delta(\mathbf{r} - \mathbf{r}_{s+}) - \delta(\mathbf{r} - \mathbf{r}_{s-})). \quad (1)$$

Equation 1 is the partial differential equation that relates the potential field ϕ to the input current I , from a dipole, through the conductivity structure of the medium σ . Here, \mathbf{r}_{s+} and \mathbf{r}_{s-} are the locations of the positive and negative current sources, respectively, and $\delta(\mathbf{r} - \mathbf{r}_s)$ is the dirac delta function, centered at the current source location. In order to solve equation 1, the problem is approximated on a discretized grid, and solved numerically. We have chosen to discretize the system using a cell-centered, variable-grid, finite volume approach, similar to that presented by Haber et al. (2000a). This yields the discretized form of equation 1:

$$(\mathbf{D} \cdot \mathbf{S}(m) \cdot \mathbf{G})\mathbf{u} = \mathbf{A}(m)\mathbf{u} = \mathbf{q}$$

$$\text{where } \mathbf{A}(m) = (\mathbf{D} \cdot \mathbf{S}(m) \cdot \mathbf{G}). \quad (2)$$

Here, \mathbf{D} and \mathbf{G} are matrices representing 3D second order finite difference divergence and gradient operators, respectively. The difference operators are applied across the entire model space, including the boundary cells. This naturally enforces no-flux boundary conditions at the edges of the model space. Although these boundary conditions are not as ideal as the impedance matched boundary conditions presented in Zhang et al. (1995), they naturally fall out of the discretization, they are numerically efficient to solve, and their effects fall off as $\frac{1}{r^2}$. Furthermore, a variable grid discretization scheme allows us to push the boundaries far away from our region of interest without creating a prohibitively large model. In equation 2, \mathbf{S} is a diagonal matrix that contains the harmonic average of the conductivity of each cell face along the main diagonal, and \mathbf{u} and \mathbf{q} are potential and source vectors, respectively, defined at the centers of the volumes. From equation 2 we see that in order to predict the potential field, we need to solve for \mathbf{u} as shown in equation 3:

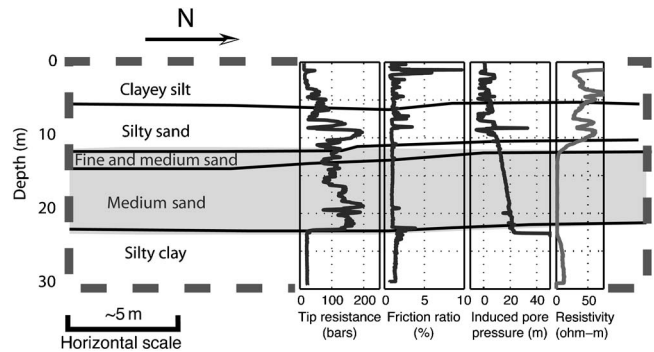


Figure 6. The RCPT data obtained from C-bert 05 at Kidd 2. The data are superimposed over the interpreted cross section for the site.

$$\mathbf{u} = \mathbf{A}(m)^{-1}\mathbf{q}. \quad (3)$$

The operator matrix \mathbf{A} is sparse and banded; therefore, equation 3 can be rapidly solved using preconditioned iterative methods.

For this work we used an incomplete LU decomposition for preconditioning. This is an expensive preconditioner to calculate; however, as \mathbf{A} remains the same for all our source terms, we can amortize the cost over all the source vectors. The solution of equation 3 was then iteratively determined, for each source vector, using a biconjugate stabilized gradient (Bicgstab) algorithm (Saad 1996).

ERT inversion

For this work, we chose to use an inexact Gauss-Newton inversion routine, similar to that described in Haber et al. (2000b). The objective function that we wish to minimize is the following:

$$\min_{\mathbf{m}} \left\{ \frac{1}{2} \|\mathbf{W}_d(\mathbf{Q}\mathbf{u} - \mathbf{d}_{\text{obs}})\|^2 + \frac{\beta}{2} \|\mathbf{W}_m(\mathbf{m} - \mathbf{m}_{\text{ref}})\|^2 \right\}, \quad (4)$$

where \mathbf{W}_d is the data weighting matrix; \mathbf{Q} is a linear interpolation operator that projects the potentials \mathbf{u} determined using equation 3 to the corresponding locations where data were acquired; \mathbf{d}_{obs} is a vector containing the observed data; \mathbf{W}_m is a model regularization matrix; β is the regularization parameter that balances the effect of data misfit and model regularization during the minimization; \mathbf{m} is our model at a given iteration, where the model parameters are $\ln(\sigma)$; and \mathbf{m}_{ref} our reference model, and in the case of the Kidd 2 data, our starting model, defined from our resistivity logs.

For the field data described here \mathbf{W}_d is a matrix that contains the estimate of the absolute error along the main diagonal as follows:

$$\text{diag}(\mathbf{W}_d) = \frac{1}{|\mathbf{d}_{\text{obs}}| \cdot SD(\mathbf{d}_{\text{obs}})}, \quad (5)$$

where $SD(\mathbf{d}_{\text{obs}})$ is the standard deviation of the observed data, obtained from stacking measurements in the field. The regularization matrix \mathbf{W}_m is an anisotropic first derivative operator. This operator promotes various levels of flatness in the x , y , and z directions. The diagonal of \mathbf{W}_m contains the relative weights of each model parameter, in particular it contains weights that penalize model structure near our current electrode locations. For our work, the regularization parameter β was set to at an initial value and progressively decreased by a factor of 10 whenever the objective function was not reduced by at least 10% between iterations.

Using the inexact Gauss-Newton method we define a starting model, \mathbf{m}_i (in this case \mathbf{m}_{ref}), that we hope is near the local minimum of equation 4. The expressions under the norms in equation 4 are linearized about this model, and we calculate a small model update $\delta\mathbf{m}$ to obtain our new solution. The update is applied to the new model as follows:

$$\mathbf{m}_{i+1} = \mathbf{m}_i + \alpha\delta\mathbf{m}, \quad (6)$$

where \mathbf{m}_{i+1} is the new model, and α is a line search parameter. The form of the Gauss-Newton update is as follows:

$$\delta\mathbf{m} = - \underbrace{(\mathbf{J}^T\mathbf{J} + \beta\mathbf{W}^T\mathbf{W})^{-1}}_{\mathbf{H}^{-1}} \times \underbrace{(\mathbf{J}^T(\mathbf{Q}\mathbf{A}(\mathbf{m})^{-1}\mathbf{q} - \mathbf{d}_{\text{obs}}) + \beta\mathbf{W}^T\mathbf{W}(\mathbf{m} - \mathbf{m}_{\text{ref}}))}_{\mathbf{g}}, \quad (7)$$

where \mathbf{J} is the Jacobian or sensitivity matrix $\left(\frac{\partial \mathbf{d}}{\partial \mathbf{m}}\right)$. The matrix \mathbf{H} is an approximation to the Hessian, while \mathbf{g} is the gradient of our objective function. It should be noted that \mathbf{J} is a very large, dense matrix, and thus, from a computational point of view, we want to avoid explicitly forming the matrix. However, it was shown in Haber et al. (2000b) that \mathbf{J} has the form

$$\mathbf{J} = \mathbf{Q}\mathbf{A}^{-1}\mathbf{B}, \quad (8)$$

where $\mathbf{B} = \frac{\partial(\mathbf{A}(\mathbf{m})\mathbf{u})}{\partial \mathbf{m}}$. The matrices \mathbf{B} and \mathbf{Q} are sparse matrices. We can see from equation 8 that we can calculate the product of the sensitivity matrix and a vector (or its adjoint) by solving the forward (described by equation 3) or adjoint problems along with two matrix multiplications. Because of this, we do not compute the Hessian explicitly but instead perform a series of matrix-vector products. The procedure for calculating \mathbf{J} is as follows:

- 1) Calculate $\mathbf{w} = \mathbf{B} \cdot \mathbf{v}$
- 2) Solve $\mathbf{x} = \mathbf{A}(\mathbf{m})^{-1}\mathbf{y}$ using Bicgstab.
- 3) Calculate $\mathbf{J} \cdot \mathbf{v} = \mathbf{Q} \cdot \mathbf{x}$

With this in mind, a natural way to solve equation 7 is by using the preconditioned conjugate gradient method (PCG), where only matrix-vector products need to be computed. Note that each PCG iteration involves one forward solve and one adjoint solve. In addition, we have to perform one forward solve and one adjoint solve in order to evaluate the gradient \mathbf{g} (Haber et al., 2000b).

The data from the RCPT logs, obtained coincidentally with the C-bert data, were included as constraints in the inversion. These data can be added to the inversion by either setting the values of the cells to their known value or as softer information by using them in the penalty function \mathbf{W}_m . For our work, we chose to include these data in the penalty function; this is done by applying a large model weight at the RCPT locations and applying no model update at these locations.

After each model update, the objective function is reevaluated, and the line search parameter α is determined to ensure sufficient decrease of the objective function. The line search parameter α starts at a fixed value (usually one) and is reduced until the objective function satisfies the Armijo inequality:

$$\Phi(\mathbf{m}_{i+1}) = \Phi(\mathbf{m}_i + \alpha\delta\mathbf{m}) \leq \Phi(\mathbf{m}_i) + c_1\alpha \nabla \Phi(\mathbf{m}_i)^T \delta\mathbf{m}, \quad (9)$$

where c_1 is a constant, that in practice takes a very small value, for example 10^{-4} and Φ is the value of the objective function. After the line search, if equation 4 has been minimized to the desired tolerance the inversion is terminated, otherwise another iteration is performed. Additionally, we use the gradient term \mathbf{g} in equation 7 as a convergence indicator; once the gradient \mathbf{g} becomes small, no further improvements can be obtained with additional iterations. For our field data, we had an excellent starting model from the RCPT logs, and thus convergence was usually obtained within three to five iterations of equation 7. This highlights another advantage of C-bert: we have high-resolution logs to construct a good starting model. We note that these inversions results are nonunique. By combining an informed starting model, an informed reference model and resistivity logs as constraints, we substantially reduce the pool of plausible solutions. This yields better results than using any of this a priori information independently.

The cone effect

One of the major challenges in working with C-bert data is that the cone, and the cone push rods are highly conductive and represent a large conductivity perturbation to the potential field near the measurement location. Unfortunately, explicitly modeling the cone-effect during inversions is computationally cost prohibitive for three reasons. First, the forward problem involves a solution at many spatial scales. Boundary effects, the survey scale (i.e., the scale at which we wish to obtain results), and the cone effect need to be modeled at different length scales. These scales range from hundreds of meters for boundary effects, to subcentimeters for the cone effect. The multiscale nature of the problem results in forward problems that, even with a variable grid mesh, can lead to models that have millions of cells. Second, the cone has a conductivity of approximately 10^6 S/m. Consequently, including it in the forward operator can greatly increase the condition number of the matrix, making the problem difficult to solve. Third, at each new measurement location, the conductivity structure of the model space is slightly different from the previous location, and thus, there is a new forward model required for each cone location. The first two issues make running a single, realistic forward model a challenging task. The third issue, that of being faced with thousands of these forward models in the inversion, makes explicitly modeling the cone infeasible.

In an effort to address the first two computational difficulties, we developed a grid refinement method for solving the forward problem. This method allows us to realize a decrease in the computational time required to solve the forward problem by an order of magnitude. Our solution approach, iteratively determined boundary conditions (IDBC), is described schematically in Figure 7. We begin by defining a fine scale conductivity model for which we would like to determine the potential field. The first step of IDBC is to define a starting grid that is coarser than our desired scale, with the boundaries far away from our region of interest. Using the conductivity values from our predefined fine scale conductivity structure, we parameterize the coarse grid by upscaling from the fine structure. We solve for the potentials \mathbf{u}_c on the coarse grid. A second grid g_m is then constructed with cell dimensions that are half of g_c , and the known conductivities are upscaled onto this grid. We then interpolate \mathbf{u}_c onto this new grid, and the potentials in the boundary cells are fixed at the interpolated \mathbf{u}_c values. The boundary conditions of this new system are now set to the interpolated \mathbf{u}_c values, and are thus more accurate than the original no-flux boundaries. We note that the new grid, although having higher resolution than the first grid, spans a smaller space, and thus, the solution has the same computational cost as for the coarse grid. We solve for the potentials on this second grid, which yields the potential field \mathbf{u}_m . Successive grids are created, parameterized, and solved until we reach our desired level of discretization. Although this approach results in many forward solutions, each model is comparatively small with respect to solving the entire finely discretized model at once, and the approach results in substantial computational savings. We note, that this approach bears some resemblance to the multigrid method in the sense that we solve the problem on progressively finer grids. Multigrid is an iterative solver for the linear system. The IDBC solution is a method for determining more accurate boundary conditions, and thus minimizing the size of the linear system we are solving. IDBC still requires an iterative solver to obtain a solution to the linear system.

Figure 8 is a plot of the results for a dipole in a 3D homogenous 100 ohm-m conductivity structure. The potential fields were deter-

mined using the fully parameterized approach as well as the IDBC approach. The potentials were converted to resistivities using the geometric factor obtained from the analytical solution to a dipole in a homogenous half-space. Both solutions have an average resistivity that is slightly above 100 ohm-m. Using the IDBC, the apparent resistivity has approximately 1% greater error than the full solution; however, since the noise level in the data is usually larger than this, the error does not affect our inverse calculations, giving us an order of magnitude increase in speed.

Although the IDBC approach allowed substantial computational savings, it is still too slow to explicitly solve for the cone effect. As mentioned above, the third issue with determining the cone effect explicitly in the inversion requires that we calculate a correction for each measurement location during each inverse iteration. Practically speaking, this would require tens of thousands of forward solutions to complete the inversion. Recognizing this, we used IDBC as a way of calculating an approximate correction for the cone effect.

Assuming that $\sigma_c \gg (\sigma_0 \text{ and } \sigma_1)$, where σ_c is the conductivity of the cone, σ_0 is the layered conductivity structure obtained from the resistivity log, and σ_1 is a conductivity structure that is locally (i.e., near the cone) the same as σ_0 (but may differ at a distance), we can develop the following correction:

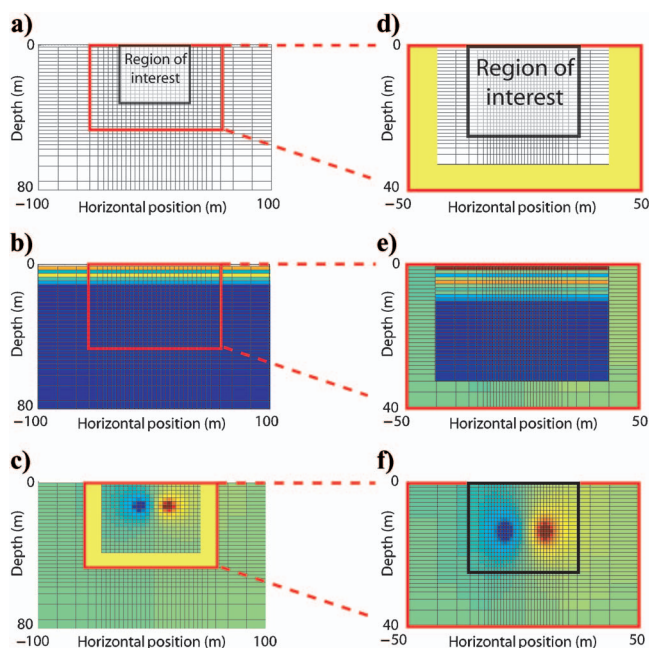


Figure 7. Schematic of the iteratively determined boundary conditions approach (IDBC), using two iterations. (a) Large coarse grid is defined with boundaries sufficiently far away so as not to influence the region of interest (ROI). (b) High-resolution resistivity logs, or the fine scale 3D resistivity structure, are upscaled onto the coarse grid. (c) The potential field is determined at every point in the volume. (d) Fine scale grid defined with cell dimensions that are $\frac{1}{2}$ of coarse grid. Potentials from the coarse grid solution [the yellow region in frame (c)] are interpolated onto the boundary cells of the fine grid. (e) High-resolution resistivity logs are upscaled onto the new grid; however, the boundary cells remain fixed potential boundaries. (f) Final solution is computed on the fine scale grid yielding a fine scale solution in the ROI.

$$u_i(\sigma_1 + \sigma_c) - u_i(\sigma_1) = u_i(\sigma_0 + \sigma_c) - u_i(\sigma_0), \quad (10)$$

where u_i is the potential for a given model point. Following from equation 10, we obtain

$$u_i(\sigma_1 + \sigma_c) = 1 + \frac{u_i(\sigma_0 + \sigma_c) - u_i(\sigma_0)}{u_i(\sigma_1)}. \quad (11)$$

If we assume that near the cone $\sigma_1 \approx \sigma_0$, which is reasonable because σ_0 was derived from the resistivity logs, we can approximate the cone effect with the following equation:

$$u_i(\sigma_1 + \sigma_c) \approx 1 + \underbrace{\frac{u_i(\sigma_0 + \sigma_c) - u_i(\sigma_0)}{u_i(\sigma_0)}}_{C_i}, \quad (12)$$

where C_i is the cone correction factor.

From equation 12 we see that by comparing the potential field obtained from a forward model $u_i(\sigma_0 + \sigma_c)$ that explicitly includes the conductivity structure of the cone, with the potentials obtained from a model that does not include the cone conductivity structure $u_i(\sigma_0)$, we can determine the modeling error associated with neglecting the cone in our model. For a new conductivity structure σ_1 , that is a perturbation about σ_0 , we can use equation 12 to approximate the potential field including the cone effect $u_i(\sigma_1 + \sigma_c)$ without explicitly calculating the cone effect for the new conductivity structure σ_1 . As described above, the inversion algorithm is based on a linearization of the nonlinear problem, and therefore, we implicitly assume that our starting conductivity structure, for example σ_0 , is close to the true conductivity. In the case of C-bert, this a reasonable assumption be-

cause our starting model σ_0 is derived from the resistivity logs. With this in mind, we recognize that calculating the correction factor before the inversion is a reasonable approach, because the starting model for our inversion is close to the final model. Thus, if we calculate a correction factor for the starting model, it will be approximately correct for our final model. Moreover, forward modeling demonstrated that the magnitude of the cone effect was largely a function of the conductivity structure immediately adjacent to the cone.

To practically implement this correction, we created a high-resolution layered model, based on the RCPT log, for each C-bert survey location. This model can be considered locally correct because it is derived from the RCPT logs. Using IDBC, we calculated the cone effect at all measurement locations for each cone profile, solving on a final grid that has cells around the cone location that are 10 mm on a side. We then calculated the correction factor C_i , as shown in equation 12. The correction factor was incorporated into the interpolation operator \mathbf{Q} , described in equation 4, thereby approximating the cone effect when the potentials are mapped to the data locations in the inversion.

Figure 9a is an example of a resistivity structure that we would obtain from an RCPT log. If we assume that the log represents a layered system, as depicted in Figure 9a, we can use the IDBC approach to calculate the C-bert data that we would obtain, while pushing the cone into the subsurface, with and without explicitly including the cone and cone rods. Figure 9b shows the results from such an experiment for a single current pair. As can be seen in Figure 9b, neglecting the presence of the cone significantly changes our calculated data. Using the data presented in Figure 9b, we can generate a cone correction factor, as described above, and apply this correction to a different data set. Figure 9c shows a resistivity structure that is identical to the one presented in Figure 9a, except for the presence of a conductivity body a small distance from the cone location. As in Figure 9b, we present modeled data that consider the cone, and modeled data that ignore the cone; in addition, we include the results of applying the cone correction to the data that do not include the cone. The corrected data set is a good approximation to the data that explicitly include the cone. Although this approximation works well for this case, we stress that in the absence of a good local resistivity estimate (e.g., the resistivity logs) this approach will not work. The correction is a linearization about the calibration model (e.g., the resistivity model in Figure 9a). If the true model is far from the calibration model, the linearization is not a good approximation and the correction will fail.

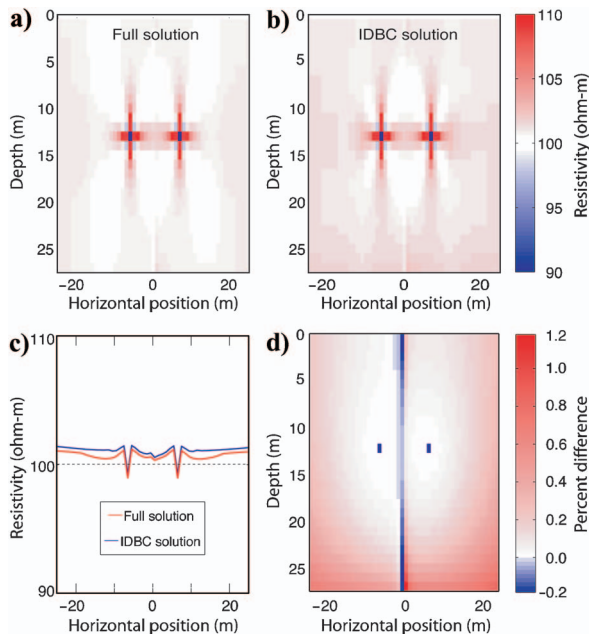


Figure 8. Comparison of IDBC solution versus the fully parameterized solution; the solutions are for a dipole in a homogenous 100 ohm-m media. The geometric factor has been applied to the potential fields, and thus, the entire image should be 100 ohm-m. (a) 2d slice through the center of the 3D solution using the full solution method. (b) The same slice as in (a) solved using the IDBC approach. (c) The vertically averaged resistivities from (a) and (b). (d) A percent difference map between (a) and (b).

Kidd 2 inversion results

For the Kidd 2 data set, we parameterized the inversions on a 240 000 cell grid. The region of interest, a volume approximately $30 \times 35 \times 30$ m, contained approximately 74 000 cells with dimensions of 0.75 m on a side. The remainder of the cells served to ensure that we encountered minimal boundary effects. We ran multiple inversions of the C-bert data that used slightly different regularization operators, as well as different initial guesses, and different starting values for the regularization parameter. The inversions tended to produce very similar results, and so we only show one of the results here.

The starting model we used was based on the four resistivity logs. Due to a problem with the RCPT logging system, the resistivity log from C-bert 01 was discarded. The model was generated by first vertically upscaling each of the logs to 0.75-m grid cells, using geomet-

ric averaging. The four upscaled logs were arithmetically averaged in the horizontal direction to create a layered starting model. Following this, the model values at the four resistivity log locations were set to the values from the corresponding upscaled logs.

Figure 10 presents inversion results for the Kidd 2 data set. From these results, we identify three resistivity units: the upper fresh water saturated region of clayey silt and silty sand, from approximately 1 to 10 m; the saltwater intrusion from 10 to 22 m; and the silty clay, below 22 m. As can be seen from the five slices, the results are dominantly layered with small horizontal variations within each layer.

At approximately five meters deep in Figure 10c and d we see a low-resistivity feature. As can be seen in Figure 10c, the RCPT log suggests that the resistivity should be higher than the inversion would suggest. A possible interpretation of these discrepancies could be the different frequencies at which the two data types were obtained; the resistivity log is obtained at 1000 Hz while the imaging data are acquired at 4 Hz. However, the work of Lesmes and Frye (2001) indicates that the resistivity variation with frequency is quite small at these frequencies. Closer examination of the CPT data (tip resistance, sleeve friction, and induced pore pressure), indicates that there are some thin silty clay layers around 5.5 m. The resistivity of these layers is being averaged differently by the two resistivity techniques (the resistivity log and the inversion). The true resistivity likely lies somewhere between the values provided by the resistivity log and the inversion. Without the coincident data, this interpretation would be difficult to make. Acquiring multiple data types is one of the largest benefits of C-bert.

C-BERT NUMERICAL EXPERIMENT

While the results of the field test are very encouraging, we recognize that the large scale structure at the Kidd 2 site is dominantly layered. We thus wanted to conduct a more challenging numerical experiment to further explore the potential benefits of C-bert.

Figure 11 is a schematic displaying the hypothetical field situation. A factory is suspected of leaking contaminants into the ground beneath the factory. The presence of the factory makes it impossible to perform a surface-based geophysical survey over the region of interest. As the plume does not extend laterally, direct sampling in boreholes would not indicate the presence of the contaminant. Furthermore, as this is a reconnaissance survey, we do not want to incur the costs and risks associated with drilling boreholes. We therefore use C-bert to establish if indeed the factory is releasing contaminants.

The model that was used for this experiment has a homogeneous 100 ohm-m background resistivity which would correspond to a freshwater

sandy aquifer. The contaminant saturated soil is modeled as a 5-ohm-m material. These values yielded a resistivity contrast similar to that found at the Kidd 2 site. The model space had 13 200 cells; the contaminant occupied 116 cells. The position of the contaminant can be seen in Figure 11. In this experiment eight permanent current electrodes were pushed into the subsurface; Figure 12 illustrates the positions of the electrodes. Following the emplacement of these

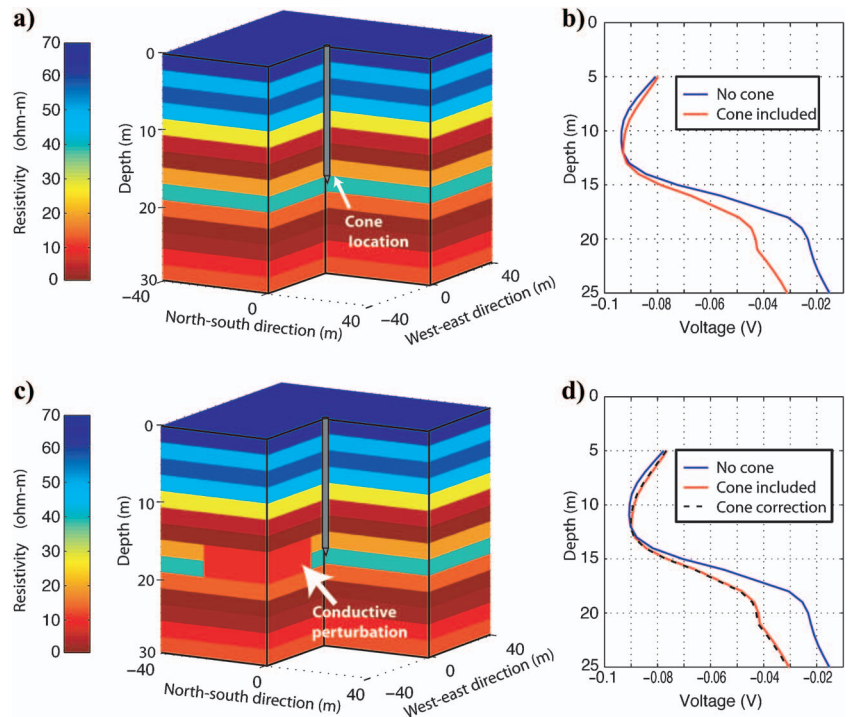


Figure 9. (a) An example of a calibration resistivity structure. (b) Calculated data for the resistivity structure in (a). (c) A perturbed resistivity structure. (d) Data calculated for the resistivity structure in (c).

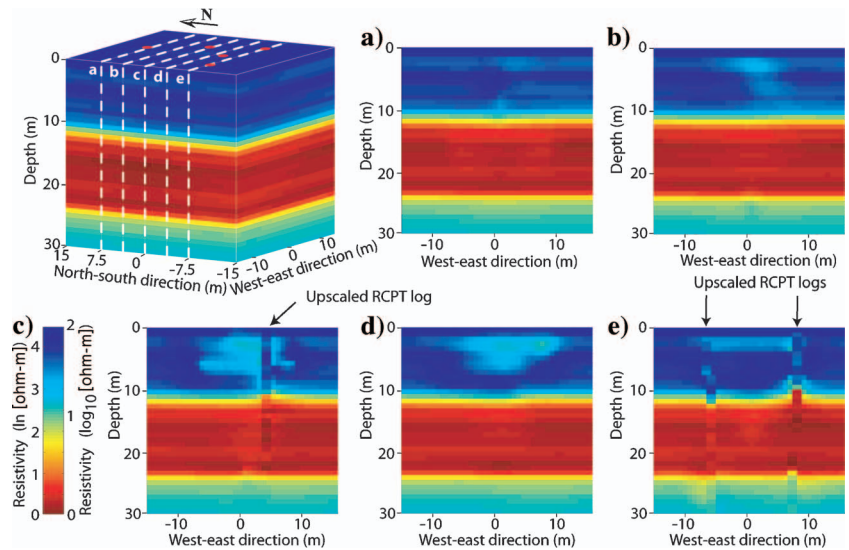


Figure 10. Results from the inversions of the Kidd 2 data set. Frames a-e are slices from the 3D solution. In frames c and e, the upscaled RCPT logs are superimposed over the inversion results. In the upper 10 m of frame c there is a discrepancy between RCPT logs and the inversion results.

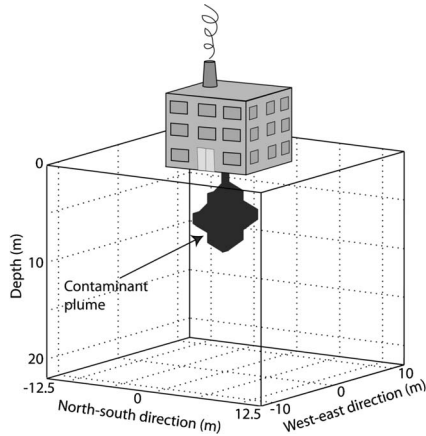


Figure 11. Schematic of the synthetic problem. There is a suspected leak directly beneath the factory.

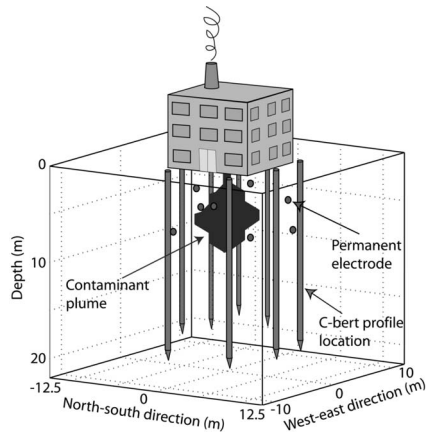


Figure 12. Eight permanent electrodes are placed around the perimeter of the factory. Four are situated at depths of 4 m and four are placed at 8 m. Eight C-bert profiles are acquired around the perimeter, as indicated by the figure. C-bert profiles were acquired to a depth of 20 m.

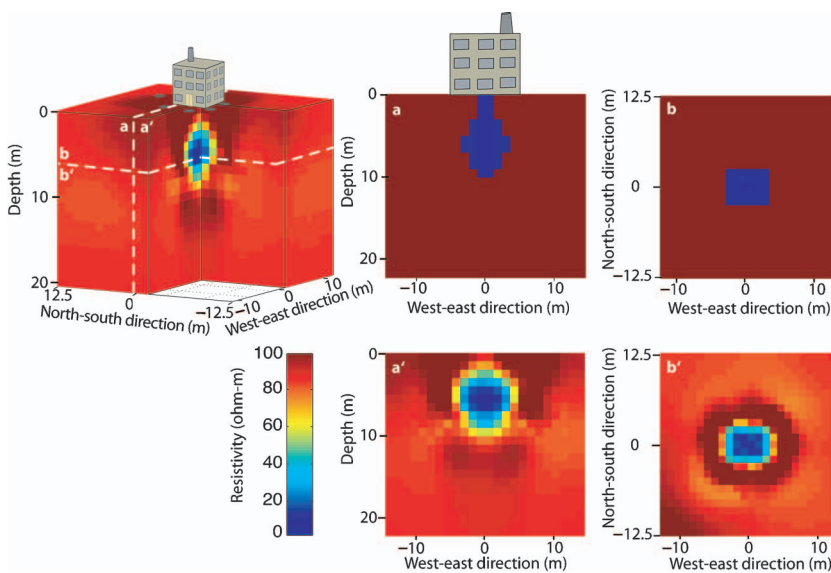


Figure 13. Inversion results for the synthetic experiment. Frames a and a' are west-east slices through the synthetic model and the inverse result, respectively. Frames b and b' are depth slices, at 6 m, through the synthetic model and the inverse results, respectively.

electrodes, we obtained a series of eight C-bert data sets around the perimeter of the building. The C-bert locations can be seen in Figure 12. A total of 4704 synthetic data points, 168 points for each of the 28 independent current pairs, were calculated using the forward modeling algorithm described above; these data were corrupted with 3%, uniformly distributed, random noise. Data were inverted using the Gauss-Newton algorithm, described earlier. As with the field experiment, we used the RCPT logs to construct our starting model. However, as the cone never directly encounters the contaminant, the logs would suggest that the starting model for the inversion be a homogeneous 100 ohm-m model. We used an isotropic flatness filter in the regularization.

Figure 13 illustrates the results of the inversion. As can be seen in the figure, we clearly identified the presence of the contaminant below the factory. This reconnaissance type of experiment highlights a major potential benefit of C-bert, that is real-time experimental design. All the RCPT data can be plotted in real time, so based on these data, one can adapt the field sampling plan as more data come to light. Furthermore, as computational speed increases, we will eventually be able to invert the C-bert data in the field, giving us 3D information that can be used to guide and adapt our survey design. For this example, if it were found that the contaminant was migrating laterally, we could quickly adapt our sampling strategy, and acquire C-bert data sets that would allow us to image the migration. The results of a survey such as this may help to rapidly design a plan for clean-up at the site. In addition, these results could be used to guide the emplacement of a more expensive, permanent ERT array for long term monitoring.

SUMMARY AND CONCLUSIONS

The focus of this work was an assessment of a cone-based imaging system for obtaining 3D images of electrical conductivity. Cone-based imaging is advantageous for several reasons. First, it is a minimally invasive way to obtain information about the subsurface 3D conductivity structure. Second, using a small number of source terms (e.g., for the Kidd 2 study there were a total of only 36 current pairs), while measuring multiple data points, can potentially result in faster inversions. Third, we obtain multiple colocated data, which better constrains inverse results and assists in interpretation. Finally, field acquisition of C-bert data lends itself well to real time experimental design allowing one to choose new test locations as more information comes to light.

The Kidd 2 field study has successfully demonstrated that C-bert data can be used to image the near subsurface. We have outlined the required field equipment and testing procedures necessary for acquiring these data. The equipment used for this survey required minor modifications of existing RCPT systems. Interpretation of the data, however, required the development of a cone-effect correction, which in turn required a computationally efficient solution to the forward problem. The iteratively determined boundary conditions approach, IDBC, was developed to facilitate this correction, by allowing us to solve the forward problem considerably faster than with a fully parameterized approach. The use of IDBC extends

beyond simply solving for the cone effect; it can be used as an effective solver for the general Poisson's equation.

While in this pilot study we collected only five C-bert data sets, we could easily obtain tens of C-bert data sets in a full-scale field survey. The RCPT logs associated with each of these C-bert data sets are not only valuable for building an accurate starting model, but also give us the potential to generate more informed regularization operators for our inversions. In over-parameterized inverse problems we must inject some a priori knowledge in order to solve them. A priori knowledge, based on in-situ, site specific measurements, is more desirable than derivative type filters, but in general, these measurements are difficult to obtain. The colocated data that are acquired during the C-bert process serve this purpose. As shown with our work, they can be used as constraints within our regularization operators, and to construct an informed reference model that is used in the regularization.

We were very encouraged by the results of the field test at the Kidd 2 site. We recognized, however, that the relatively simple layered structure at the site did not allow us to fully demonstrate the potential benefits of C-bert. Our synthetic example illustrates the ability of C-bert to determine conductivity values in regions that are not readily accessible to other forms of measurement. We believe that, with further refinement, C-bert will become a useful tool for acquiring subsurface conductivity images.

ACKNOWLEDGMENTS

Partial funding for this project came from a McGee grant, from the School of Earth Sciences at Stanford University and a DOE Grant through Emory University (DOE CAREER Grant DE FG02 05ER25696). We thank John Howie for the use of the UBC Department of Civil Engineering cone truck, and for his input on the interpretation of the RCPT data. The field work would not have been possible without the assistance of Ali Amini and Scott Jackson from the UBC Department of Civil Engineering. We extend thanks to three reviewers for providing such excellent reviews of this paper; their contributions greatly enhanced this manuscript. In particular we thank Partha Routh, who completed a detailed review and provided the derivation for the cone correction that has been included in this paper.

REFERENCES

- Binley, A., G. Cassiani, R. Middleton, and P. Winship, 2002, Vadose zone flow model parameterisation using cross-borehole radar and resistivity imaging: *Journal of Hydrology*, **267**, 147–159.
- Campanella, R. G., and I. Weemes, 1990, Development and use of an electrical resistivity cone for groundwater contamination studies: *Canadian Geotechnical Journal*, **27**, 557–567.
- Clague, J. J., J. L. Luternauer, and R. J. Hebda, 1983, Sedimentary environments and postglacial history of the Fraser Delta and lower Fraser Valley, British Columbia: *Canadian Journal of Earth Sciences*, **20**, 1314–1326.
- Daily, W., and A. Ramirez, 1995, Electrical-resistance tomography during in-situ trichloroethylene remediation at the Savannah river site: *Journal of Applied Geophysics*, **33**, 239–249.
- Daniel, C. R., H. L. Giacheti, J. A. Howie, and R. G. Campanella, 1999, Resistivity piezocone (RCPTU) data interpretation and potential applications: *Proceedings of the XI Panamerican Conference on Soil Mechanics and Geotechnical Engineering*, 361–368.
- Haber, E., U. M. Ascher, D. A. Aruliah, and D. W. Oldenburg, 2000a, Fast simulation of 3D electromagnetic problems using potentials: *Journal of Computational Physics*, **163**, 150–171.
- Haber, E., U. M. Ascher, and D. Oldenburg, 2000b, On optimization techniques for solving nonlinear inverse problems: *Inverse Problems*, **16**, 1263–1280.
- Hofmann, B. A., 1997, In situ ground freezing to obtain undisturbed samples of loose sand for liquefaction assessment: Ph.D. thesis, University of Alberta.
- Hunter, J. A., S. E. Pullman, R. A. Burns, R. L. Good, J. B. Harris, A. Pugin, A. Skvortsov, and N. N. Goriainov, 1998, Downhole seismic logging for high-resolution reflection surveying in unconsolidated overburden: *Geophysics*, **63**, 1371–1384.
- Jarvis, K. D., and R. Knight, 2000, Near-surface VSP surveys using the seismic cone penetrometer: *Geophysics*, **65**, 1048–1056.
- , 2002, Aquifer heterogeneity from SH-wave seismic impedance inversion: *Geophysics*, **67**, 1548–1557.
- Jarvis, K., R. J. Knight, and J. A. Howie, 1999, Geotechnical applications of VSP surveys using the seismic cone penetrometer: *Proceedings of the Symposium on the Application of Geophysics to Engineering and Environmental Problems*, 11–20.
- Kenna, A., J. Vanderborght, B. Kulesa, and H. Vereecken, 2002, Imaging and characterisation of subsurface solute transport using electrical resistivity tomography (ERT) and equivalent transport models: *Journal of Hydrology*, **267**, 125–146.
- LaBrecque, D. J., and X. Yang, 2001, Difference inversion of ERT data; A fast inversion method for 3-D in situ monitoring: *Journal of Environmental & Engineering Geophysics*, **6**, 83–89.
- Lesmes, D. P., and K. M. Frye, 2001, Influence of pore fluid chemistry on the complex conductivity and induced polarization responses of Berea sandstone: *Journal of Geophysical Research*, **106**, 4079–4090.
- Lunne, T., P. K. Robertson, and J. J. M. Powell, 1997, *Cone penetration testing in geotechnical practice*: Blackie Academic & Professional.
- Narbutovskih, S. M., W. D. Daily, R. M. Morey, and R. S. Bell, 1997, Test results of CPT-deployed vertical electrode arrays at the DOE Hanford Site: *Proceedings of the Symposium on the Application of Geophysics to Engineering and Environmental Problems*, 21–31.
- Neilson-Welch, L., 1999, Saline water intrusion from Fraser River estuary: A hydrogeological investigation using field chemical data and a density-dependent groundwater flow model: M.S. thesis, University of British Columbia.
- Neilson-Welch, L. and L., Smith, 2001, Saline water intrusion adjacent to the Fraser River, Richmond, British Columbia: *Canadian Geotechnical Journal*, **38**, 67–82.
- Saad, Y., 1996, *Iterative methods for sparse linear systems*: PWS Publishing Company.
- Singha, K., and S. M. Gorelick, 2005, Saline tracer visualized with electrical resistivity tomography: Field scale spatial moment analysis: *Water Resources Research*, **41**, W05023.
- Slater, L., A. M. Binley, W. Daily, and R. Johnson, 2000, Cross-hole electrical imaging of a controlled saline tracer injection: *Journal of Applied Geophysics*, **44**, 85–102.
- Slater, L., A. Binley, R. Versteeg, R. G. Cassiani, R. Birken, and S. Sandberg, 2002, A 3D ERT study of solute transport in a large experimental tank: *Journal of Applied Geophysics*, **49**, 211–229.
- Versteeg, R., R. Birken, S. K. Sandberg, and L. Slater, 2000, Controlled imaging of fluid flow and a saline tracer using time lapse GPR and electrical resistivity tomography: *Proceedings of the Symposium on the Application of Geophysics to Engineering and Environmental Problems*, 283–292.
- Zhang, J., R. L. Mackie, and T. R. Madden, 1995, 3-D resistivity forward modeling and inversion using conjugate gradients: *Geophysics*, **60**, 1313–1325.